
Article:
Sun, L., Muszka, K., Wynne, B.P. orcid.org/0000-0001-6536-7004 et al. (1 more author) (2017) Influence of strain reversal on dynamic transformation in microalloyed steels deformed above the Ae₃ temperature. Journal of Materials Science. ISSN 0022-2461

https://doi.org/10.1007/s10853-017-1352-7

Influence of strain reversal on dynamic transformation in microalloyed steels deformed above the Ae_3 temperature[1]

L. Sun[a,*], K. Muszka[b], B.P. Wynne[c] and E.J. Palmiere[c]

a) Department of Materials Science and Metallurgy, University of Cambridge, 27 Charles Babbage Road, Cambridge, CB3 0FS, UK

b) Faculty of Metals Engineering and Industrial Computer Science, AGH University of Science and Technology, Mickiewicza 30, 30-059 Krakow, Poland

c) Department of Materials Science and Engineering, The University of Sheffield, Sir Robert Hadfield Building, Mappin Street, Sheffield, S1 3JD, UK

*Corresponding author, current address: GE Power, Newbold Road, Rugby, CV21 2NH, UK, email: L.Sun@cantab.net

Abstract:

In the present work, the effect of strain path reversals on dynamic transformation (DT) above Ae3 temperature was studied using an API grade X-70 microalloyed steel deformed by torsion with single and multiple strain path reversals. The results revealed the important role played by strain path reversals on influencing the evolution of austenite grain boundaries through inhomogeneous deformation, therefore, affecting DT behaviours. In addition to flow stress-strain analysis and microstructure investigation, Finite Element Method (FEM) combined with 3D Digital Materials Representation (DMR) approach was used to gain insights to the effects of deformation with strain path reversals on the development of microstructural features in the prior austenite grains.

Keywords: Thermomechanical processing; Low-carbon steel; High-temperature deformation; Grain boundaries (GBs); Solid-state phase transformation

[1] Pre-print for publication in Journal of Materials Science 2017, DOI: 10.1007/s10853-017-1352-7

1 Introduction

Dynamic strain-induced transformation (DSIT) have received considerable attention in the past decade from not just academia but also industry [1-5] due to its great potential as a relative simple processing route to produce steels containing ultrafine ferrite (UFF). However, despite considerable investments made to industrialise this process, the fundamental mechanism of DSIT is still not well understood. The dynamic austenite to ferrite phase transformation generally occurs during concurrent deformation of the austenite at temperatures below or around Ae_3. The dynamic nature of DSIT was confirmed by in situ X-ray diffraction studies [6, 7]. Furthermore, the requirement of the minimal strain $\varepsilon_{c,DSIT}$ which is the critical strain to initiate DSIT in austenite when deforming at a certain temperature was established [8-10]. As the onset of DSIT introduces relatively soft ferrite into the austenite matrix, it was generally believed that this would be reflected on the flow stress-strain curves as well. Therefore, while the direct observation of DSIT nucleation when strained to $\varepsilon_{c,DSIT}$ remains challenging, a number of studies [11-13] successfully used the Poliak-Jonas "double-differentiation" peak method [14] to analyse the flow stress-strain curves to determine the value of $\varepsilon_{c,DSIT}$.

Very recently, several studies from different research groups also reported that dynamic transformation (DT) was observed when the deformation temperatures were above the Ae_3 [15-18]. This was probably due to the fact that plastic deformation of austenite could increase the driving force for ferrite transformation and reduce the energy barriers for ferrite nucleation, therefore, effectively raising the Ae_3 temperature of deformed austenite. The discovery of DT above Ae_3 could have a profound impact on accelerating the commercial application of the DT processing methods. By far the biggest obstacle is that the roll force required to produce large reductions at low temperatures below Ae_3 exceeds the capacity of current rolling technology. Although innovative processing technology such as "Super Short Interval Multi-pass Rolling Process" has been developed [2], full commercial application remains challenging. If the production of ultrafine ferrite

steel can be achieved via a DT/DSIT process at temperatures close to or above the Ae_3, the required roll force could be significantly reduced. However, at higher temperatures, substantial larger reduction might be needed to achieve the required ferrite grain refinement, therefore, requiring multi-pass deformation inevitably involving strain path changes. A number of studied showed that simple strain path reversal during hot working of austenite could affect the subsequent recrystallisation, precipitation and phase transformation [19, 20]. A more recent study by the authors showed that DSIT can be completed suppressed by strain path reversals even when deformed to a very high von Mises equivalent strain of 2.0 at temperatures below Ae_3 [13]. Furthermore, if the deformation temperature is high enough, dynamic recrystallisation (DRX) of austenite could be activated when deformed to high strains. As DRX nucleation takes place predominantly at austenite grain boundaries where local serration and bulging develops with straining [21], it could potentially compete with DT nucleation and undermine the effectiveness of the latter process to produce UFF steel. Microalloying elements in solid solution, particularly Nb, were reported to produce a retardation effect on DRX, resulting in higher critical strains required for its initiation [22, 23]. Therefore, DT could be better realised in microalloyed steel grades than in conventional C-Mn steels. Nevertheless, it is still necessary to understand the interactions among strain path changes, DT and DRX to further utilise DT above the Ae_3 as a commercial viable process for producing UFF steels.

In the present study, the effect of strain path reversals on DT above the Ae_3 temperature was studied using an API grade X-70 microalloyed steel deformed by torsion with single and multiple strain path reversals. In addition to flow stress-strain analysis and microstructure investigation, Finite Element Method (FEM) combined with 3D Digital Materials Representation (DMR) approach was used to gain insights to the effects of deformation with strain path reversals on the development of microstructural features in the prior austenite grains. The results revealed the

important role played by strain path reversals on influencing the evolution of austenite grain boundaries through inhomogeneous deformation, and therefore, affecting DT behaviours.

2 Experimental

2.1 Strain path testing

A commercially produced low carbon microalloyed X-70 pipeline steel was used used in this study as a representative microalloyed steel composition, containing 0.036C-1.56Mn-0.31Si-0.16Cr-0.16Ni-0.16Cu-0.039Nb-0.029Al-0.014Ti-0.005Mo-0.004V-0.008P-0.0006S (wt%). The as-received plate with a thickness of 19 mm was homogenised at 1250ºC for 3 hours in a N_2 atmosphere followed by immediate water quenching to maintain the alloy elements present at 1250ºC in solid solution. A microstructure of equiaxed austenite grains of fairly uniform diameter was achieved after the homogenisation heat treatment (micrograph can be found in REF [13]). The austenite grain size was 65.1±3.7 µm in the original rolling direction, and 65.6±4.3 µm in the transverse direction (errors represent 95% confidence intervals). Solid bar torsion specimens of 20 mm gauge length and 10 mm diameter were then machined according to the geometry given elsewhere [20, 24].

Hot torsion tests with single and multiple strain reversals were conducted using the servo-hydraulic Arbitrary Strain Path (ASP) testing machine at The University of Sheffield. The test was conducted in air as the oxidation/decarburization zone was limited to <50 µm, i.e. 1% of the gauge radius determined by metallographic examination. Specimens were heated at $12°C \cdot s^{-1}$ by an induction method to 1250°C for equilibration of 2 minutes. The specimens were then cooled at $5°C \cdot s^{-1}$ to the deformation temperature of 920°C. This is well above the A_{e3} temperature of the heat-treated and undeformed X-70 steel, which is approximately 844°C based on its chemical composition calculated using both MatCalc and JMatPro thermodynamic software. Cyclical torsion tests of two (2-pass) and eight (8-pass) passes were conducted isothermally. By applying a constant

angular speed, a constant strain rate of 1 s^{-1} was produced at the effective radius, i.e. ~72.4% of the gauge radius as schematically shown in Figure 1(a). By applying the concept of effective radius, the complexity of deriving the shear stress (hence von Mises equivalent stress) from recorded machine torque data for torsion tests can be significantly reduced. Meanwhile, the effective radius provides a basis for consistent microstructural and/or textural analysis. Detailed discussions on effective radius for solid bar torsion testing can be found in Ref [25, 26].

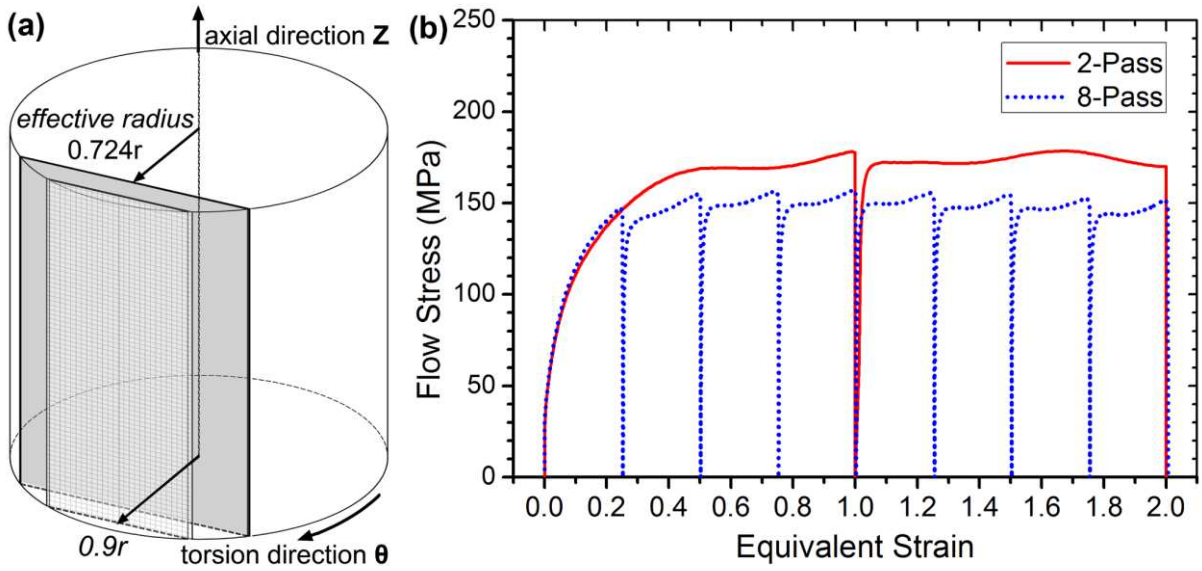

Figure 1: (a) Schematic illustration shows the position of the two planes revealed for microstructural observation at the effective radius (0.724r) and at 90% of the radius (0.9r) within the gauge section of a solid bar torsion specimen.(b) The von Mises equivalent stress–strain curves of the microalloyed steel subjected to 2-pass and 8-pass cyclical torsion tests at 920°C.

For the 2-pass test, the specimen was forward torsional deformed to a von Mises equivalent strain of 1.0 (ε_{vm}=1.0 at the effect radius), immediately followed by reverse torsion of ε_{vm}=1.0 to a total accumulative strain of 2.0, albeit a net strain of 0. The delay due to reversing the straining direction was less than 0.2 second. The 8-pass test consisted of four cycles of forward-reverse torsion with each pass of ε_{vm}=0.25, producing the same amount of accumulative strain of 2.0 and a net strain of 0. After deformation, specimens were water quenched. The delay between the end of straining and the onset of quenching was less than 0.2 seconds. The recorded cooling rate during quenching from deformation temperature 920°C to 200°C was greater than 180°C·s^{-1}. Based on

previous studies on the CCT behaviour of similar X-70 steels [27, 28], this cooling rate should be able to minimise the ferrite formation during quenching.

Metallographic specimens of tested materials were taken on the tangential plane that is normal to the radius direction (r) at the effective radius (0.724r) and at 90% of the gauge radius (0.9r) and contains the axial (Z) and shear (θ) directions of the torsion test as outlined in Figure 1(a). All microstructural observations were made along the central line of the tangential planes as schematically illustrated in Figure 1(a). Secondary electron micrographs were taken at both the effective radius and 0.9r on specimens etched by 2% Nital using a FEI InspectF FEGSEM at 20 kV. EBSD data were collected only at the effective radius on specimens mechanically polished by colloidal silica using an Oxford Instruments HKL Nordlys camera with Channel 5 software in the same FEGSEM operating at 20 kV. Typical areas of 400 µm (in Z direction) by 300 µm (in θ direction) were mapped using a step size of 0.25 µm. An indexing rate of at least 80% was achieved, then a post-acquisition noise reduction procedure outlined elsewhere was applied [29].

2.2 FEM multi-scale modelling using 3D-DMR

In order to understand better the effects of deformation with strain path reversals to the development of microstructural features in the prior austenite grains, Finite Element Method (FEM) combined with a 3D Digital Materials Representation (DMR) approach was used. The general idea of DMR is a finite element representation of microstructure with its features represented explicitly. This approach has been successfully used for simulations of deformation behaviour of various materials under a wide range of processing conditions [30-33]. In the present work, the material behaviour was described using elasto-plastic model with a combined isotropic-kinematic hardening rule [34].The evolution law of this flow rule consists of the two main components: a nonlinear kinematic hardening component which describes the translation of the yield surface in stress space through the backstress α:

$$\dot{\alpha}_k = C_k \frac{1}{\sigma_0}(\sigma - \alpha)\dot{\bar{\varepsilon}}^{pl} - \gamma_k \alpha_k \dot{\bar{\varepsilon}}^{pl},\ \alpha = \sum_{k=1}^{N} \alpha_k \quad (1)$$

where, α_k is the backstress, N, is the number of backstresses, σ_0 the equivalent stress defining the size of the yield surface and C_k and γ_k are material parameters; and an isotropic hardening component describing the change of the equivalent stress defining the size of the yield surface, as a function of plastic deformation:

$$\sigma_0 = \sigma_0 + Q_\infty(1 - e^{-b\dot{\bar{\varepsilon}}}) \quad (2)$$

where, σ_0 is the yield stress at zero plastic strain and Q_∞ and b are material parameters. A combination of kinematic and isotropic hardening rules allows not only to change the value of the radius of yield surface but also to move it within the stress space, what enables capturing such phenomena as Bauschinger effect, and hence, makes it possible to account for a proper description of the deformation behaviour during strain reversals.

Parameters of the utilised model can be specified directly, calibrated based on a half-cycle test data (unidirectional tension or compression), or can be obtained based on the test data from a stabilised cycle (when the strain-stress curve no longer changes shape from one cycle to next). In the present study, the model parameters were described using data from the torsion test provided as a half-cycle curve.

The multiscale model of the torsion test was designed according to that illustrated in Figure 2. A concurrent multiscale computing method – namely submodelling – was used here to bridge different length scales. The general idea of this approach is solving a problem first with one, coarse mesh describing the global domain; then another and generally finer mesh is used to reanalyse a certain subpart of the global domain which is of particular interest. Thus, either the displacement field or the stress field of a global domain is interpolated to the cutting boundary of a submodel having a fine mesh along the edges. In this study, the global model representing the entire geometry

of the strain gauge of the torsion sample geometry was prepared and analysed using Abaqus Standard code.

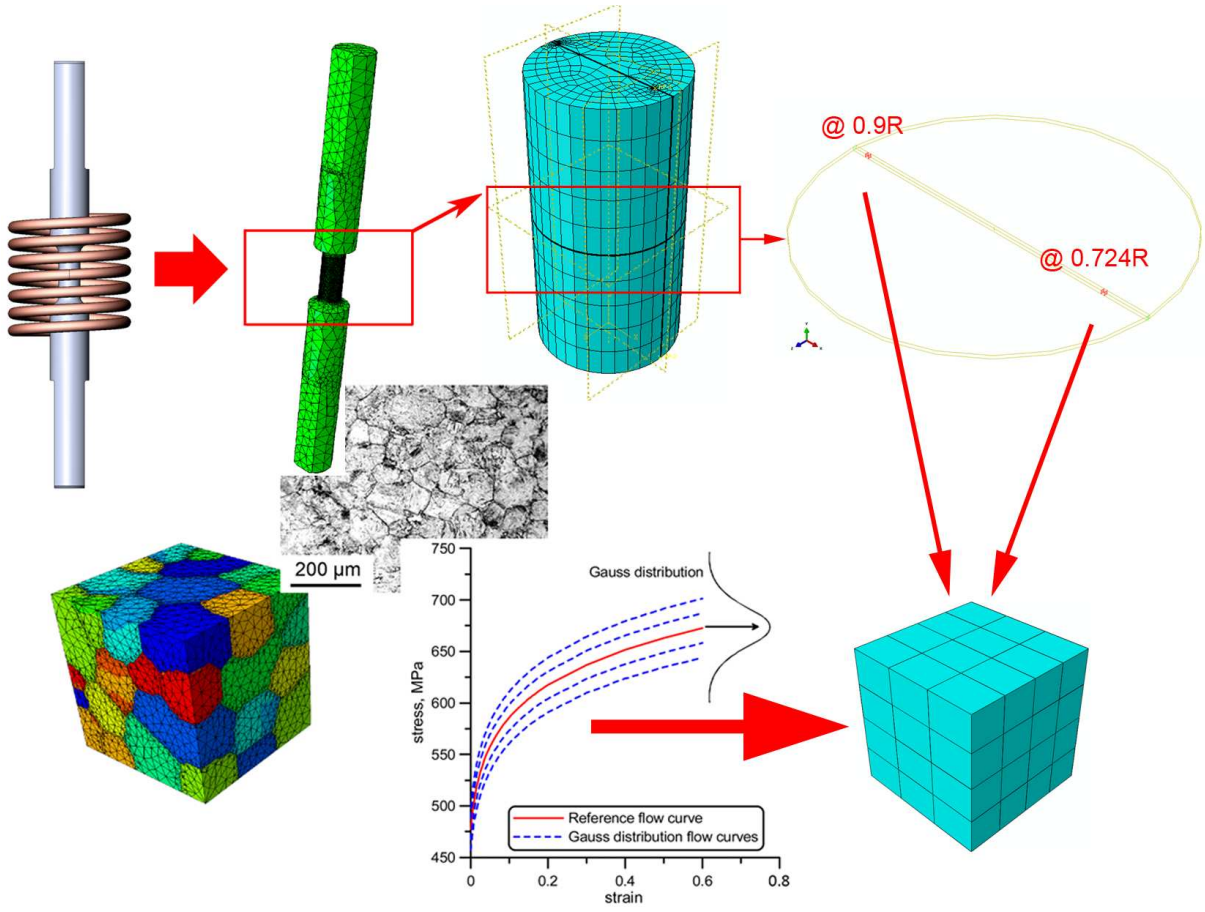

Figure 2: general concept of multiscale modelling approach utilised in the current work

Next, the submodels were generated using the DMR approach and calculations were performed again. Two unit cells (100 µm × 100 µm × 100 µm) with 37 grains each were created to capture the effect of the process on inhomogeneity of both strain and microstructure. They were placed in the positions along the gauge radius that correspond to the effective radius (0.724r) and near the surface at 0.9r. Both, flow stress data and the parameters of the combined material hardening model applied in the submodel were additionally diversified using the Gauss distribution function to reflect differences in the crystallographic orientations.

3 Results

3.1 Macroscopic flow behaviour

The recorded torque-angle data were converted to isothermal stress-strain curves using the methods outlined in Ref [25]. The results are shown in Figure 1(b). The overall flow stress during the 2-pass deformation is higher than that during the 8-pass test. Small amount of Bauschinger softening were observed upon each strain reversal for both tests. These observations are consistent with several previous studies [13, 25, 35], however to a lesser extent, probably due to the higher deformation temperature adopted in the current work as it is known that the extent of Bauschinger softening decreases with increasing deformation temperature [36, 37].

For the 2-pass test, no significant amount of work hardening was observed when strained beyond ε_{vm} of 0.5 during the forward torsion. Afterwards, a quasi-steady state was reached with small amplitude fluctuations of the flow stress with both dynamic softening and work hardening occurring. A small drop in the flow stress (~10MPa) was observed immediately after the strain path reversal. The overall trend of the flow stress during the reverse torsion remained at a similar quasi-steady state comparable to that during the forward torsion in the first pass. Furthermore, small amplitude fluctuations of the flow stress were also observed during the second pass.

As the deformation temperature of 920°C is relatively high, both DRX of austenite and DT could have occurred during deformation causing dynamic softening to the flow stress of the X-70 steel. Previously, the "double-differentiation" method developed by Poliak and Jonas [14, 38] for studying the initiation of DRX was used to determine the critical stress/strain for the onset of DT deformed at lower temperatures near or below the Ae_3 [11, 13]. The critical stress and strain condition was determined by the stationary point ($-\partial(\partial\sigma/\partial\varepsilon)/\partial\sigma=0$) on the double-differentiation curve, i.e. the derivative of strain hardening rate ($\Theta=\partial\sigma/\partial\varepsilon$) with respect to flow stress σ. The rationale is that both DT and DRX as softening mechanism are believed to affect the strain

hardening behaviour of the deformed material. Therefore, the initiation of such softening would be reflected as an inflection point on the plot of strain hardening rate ($\Theta=\partial\sigma/\partial\varepsilon$) against flow stress ($\sigma$) (i.e. the Kock-Mecking plot [39]) or as an stationary point on the "double-differentiation" curve ($\partial\Theta/\partial\sigma$ vs. σ) [11, 14]. However, a recent study by Jonas et al [40] showed that by first fitting flow curves with very high degree of polynomial equations (11 or above for the whole flow curve or at least 8 for the ascending part of the flow curve) then applying the "double-differentiation" method, two (instead of one) stationary points were found on flow curves obtained at temperatures above Ae_3. The authors attributed the first stationary point to the onset of DT and the latter one for the initiation of DRX. Assuming the above method is indeed valid, the critical conditions for DT and DRX were determined for the current work following a similar approach: Firstly, the strain hardening rate ($\Theta=\partial\sigma/\partial\varepsilon$) was plotted against the flow stress σ, from the forward torsion part of the 2-pass test (shown in Figure 3a). Secondly, the Θ-σ plot was fitted by a degree of 9 polynomial equation as shown in Figure 3(a). Finally, differentiation of the fitted polynomial curve with respect to the flow stress σ gave the "double-differentiation" curve with two stationary points as shown in Figure 3(b). This results suggests that a critical stress ($\sigma_{C,DT}$) of 137 MPa and a critical strain ($\varepsilon_{C,DT}$) of 0.20 are required for the onset of DT under the current experiment conditions. For the initiation of DRX, the critical conditions are $\sigma_{C,DRX}\approx154$ MPa and $\varepsilon_{C,DRX}\approx0.30$.

For the 2-pass deformation, the forward strain to $\varepsilon_{vm}=1.0$ in the first pass was significantly higher than both of the critical strains. Therefore, DT and possibly DRX would have been activated during the forward torsion. However, for the 8-pass test, the forward torsion to ε_{vm} of 0.25 was only marginally higher than the $\varepsilon_{C,DT}$ of 0.20, and still below the $\varepsilon_{C,DRX}$ of 0.30. As both DT and DRX are believed to be highly dependent on the increment and shape change, i.e. serration and bulging, of austenite grain boundaries; the small amplitude of forward strain (0.25) during the 8-pass test probably could not cause enough changes to the austenite grain boundaries. As a result, retardation

of DRX and DT were expected at the effective radius in the 8-pass test. This is supported by the microstructural observations presented in the following section.

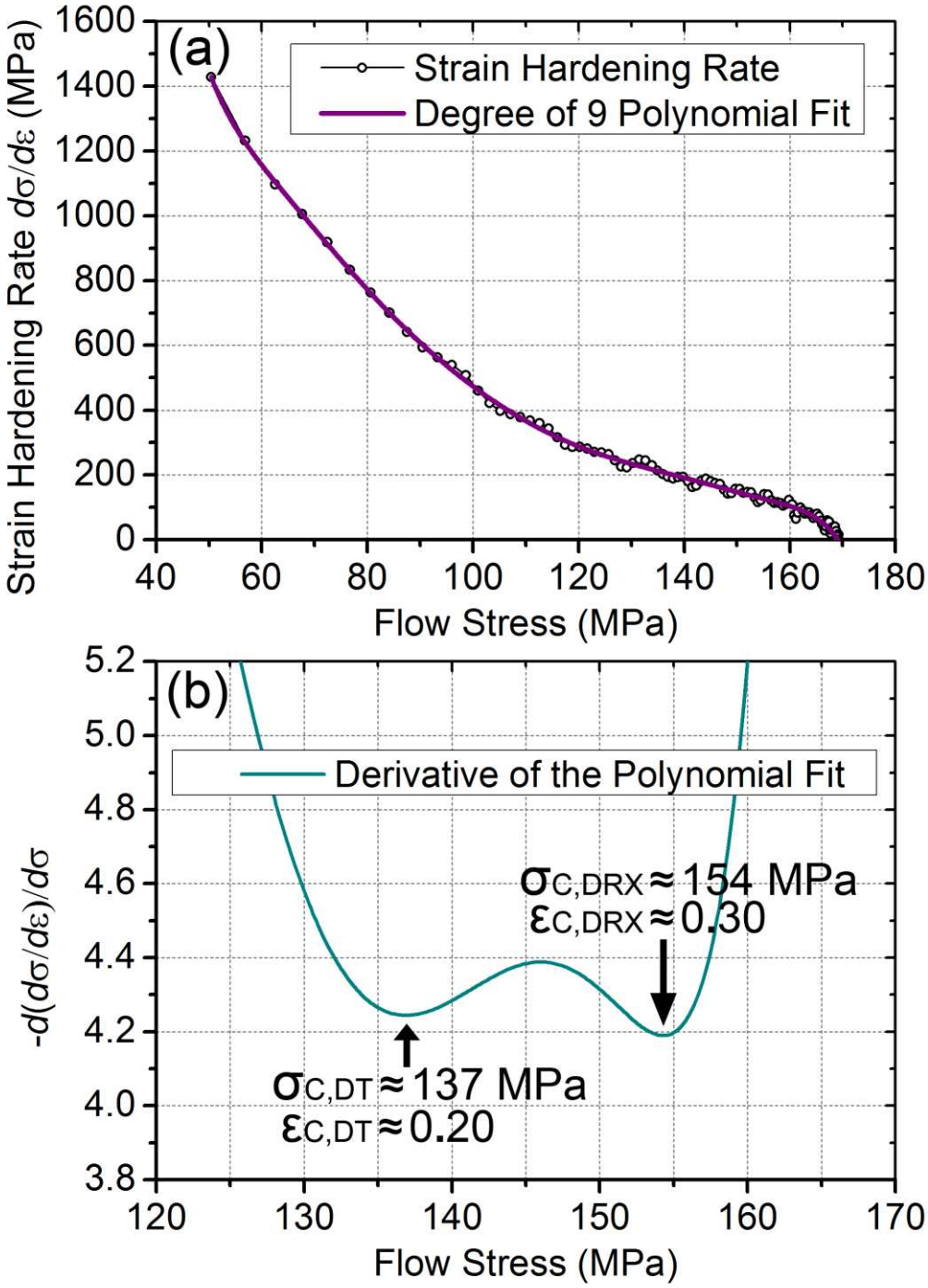

Figure 3: (a) strain hardening rate ($\Theta=\partial\sigma/\partial\varepsilon$) derived from the flow curve of the forward torsion part of the 2-pass test and its 9-degree polynomial fit plotted against the flow stress σ; (b) derivative of the polynomial fitted Θ with respect to σ showing two stationary points, which are corresponding to the onset of DT and DRX, respectively

3.2 Microstructure at the effective radius (0.724r)

3.2.1 Inverted secondary electron contrast in SEM

The microstructure of the 2-pass tested specimen is shown in Figure 4(a) and (b) by inverted secondary electron contrast from SEM. It can be seen that more than half (56.5±7.0 vol%, measured by point counting) of the austenite had already transformed to fine quasi-polygonal ferrite, which is believed to be produced by the DT mechanism during deformation. However, considerable amount of the austenite, mainly in the interior of the grains, remained untransformed after deformation. Therefore, during the rapid quenching, the remaining austenite transformed to lath martensite by displacive transformation mechanism. Such martensite can be seen in Figure 4(b) indicated by the letter M.

These observations are in broad agreement with the flow curve/work hardening rate analysis that indicates the forward torsion strain of ε_{vm}=1.0 far exceeded, in fact, is about 500% of the critical strain $\varepsilon_{C,DT}$ of 0.20 for initiating the DT. Therefore, the deformed austenite transformed to the fine ferrite grains by the DT mechanism during further straining. However, the amount of DT ferrite is much lower in the current work than the DSIT ferrite observed in a previous study of the same material tested by the same 2-pass deformation but at the lower temperature of 820°C [13].

Analysed using the "double-differentiation" method, the previous study suggested what the critical strain of DSIT at 820°C was $\varepsilon_{C,DSIT}$=0.5 [13]. Therefore, the monotonic forward strain to ε_{vm}=1.0 is only 200% of $\varepsilon_{C,DSIT}$. Yet after the 2-pass deformation, the majority of the austenite transformed to fine grained ferrite via a DSIT mechanism, only a very small fraction of austenite remained, hence producing martensite after quenching. The lower fraction of DT ferrite observed in the current work when the deformation temperature is well above the Ae_3 temperature of the X-70 steel is probably due to low chemical driving forces for phase transformation at higher temperatures, and to some lesser extend due to other dynamic softening mechanisms competing

with DT during deformation, especially the DRX of the austenite, as both DT and DRX are believed to primarily nucleate on serrated and bulged austenite grain boundaries. This will be discussed further in Section 4.1.

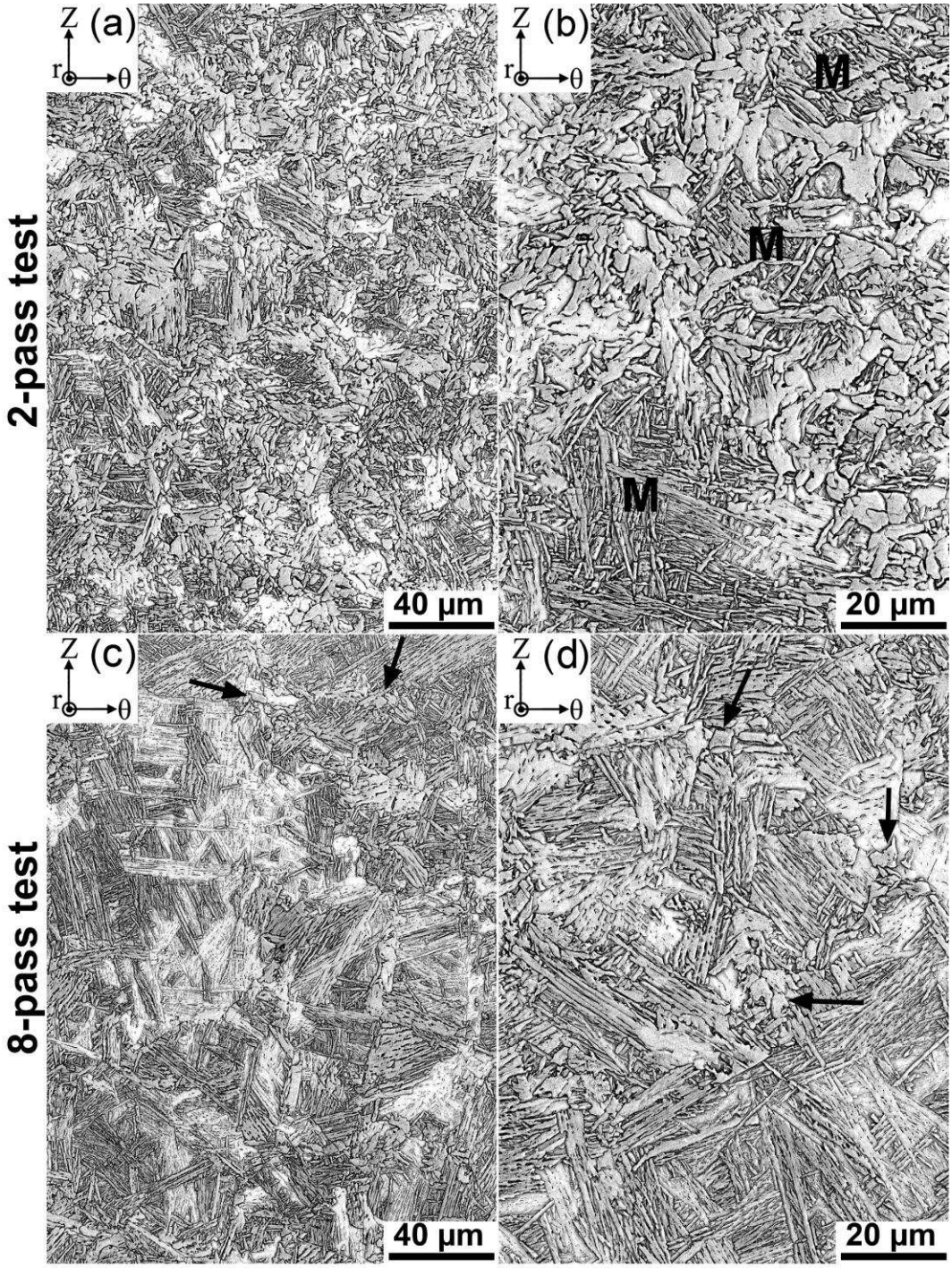

Figure 4: Micrographs showing inverted secondary electron contrast of the microstructure at effective radius in the 2-pass deformed specimen (a and b) and in the 8-pass deformed one (c and d)

Micrographs by inverted secondary electron contrast taken at the effective radius in the 8-pass deformation specimen are shown in Figure 4(c) and (d). The vast majority of the transformation products are lath martensite that was produced from quenching the untransformed austenite after deformation. A very small amount of DT ferrite was produced during the 8-pass deformation (indicated by black arrows in Figure 4c and d). Furthermore, by judging the length of the martensite lath, little DRX occurred during the deformation. The amounts (vol%) of DT ferrite after the 2-pass tested and 8-pass tested samples measured by a standard point counting method are given in Table 1. Clearly, the volume fraction of DT ferrite in the microstructure after the 8-pass test is significantly lower than that after the 2-pass test (56.5%±7.0%). These observations all indicate that DT was suppressed during the 8-pass test.

Table 1 Fractions (vol%) of dynamically transformed DT ferrite after the 2-pass and 8-pass tests at different gauge radius positions. Errors represent the 95% confidence intervals of the measurement.

		2-pass		8-pass	
Position	Total accumulative strain	Strain per pass	DT ferrite fraction (vol%)	Strain per pass	DT ferrite fraction (vol%)
Effective radius 0.724r	2.00	ε_{vm}=1.00	56.5±7.0	ε_{vm}=0.25	2.8±0.9
Near surface 0.9r	2.48	ε_{vm}=1.24	90.4±3.7	ε_{vm}=0.31	13.8±1.0

The retardation of DSIT and DRX by multiple strain reversals combined with small strain amplitude during the 8-pass deformation were previously studied using the same X-70 steel [13] and a non-transforming 316L stainless steel [25], respectively. It was established that the main reason is probably due to the forward strain to ε_{vm}=0.25 before each strain reversal is not large enough to cause enough serration and bulging of austenite grain boundaries to facilitate the DSIT or DRX [13, 25]. In the present study, the forward strain of ε_{vm}=0.25 in the 8-pass test is greater than the $\varepsilon_{C,DT}$ of 0.20 but smaller than the $\varepsilon_{C,DRX}$ of 0.30 derived by flow-curve analysis. Consequently, a

small fraction of DT ferrite was produced during forward torsion deformation before strain reversal when the monotonic strain exceeded the critical strain for DT nucleation.

3.2.2 EBSD orientation image microscopy

From the large EBSD dataset (about 400 µm by 300 µm) taken at the effective radius, a smaller subset is used to plot various maps to highlight the typical microstructural features of the transformation products. These maps are given in Figure 5 for the specimen deformed in 2-passes and in Figure 6 for the specimen deformed in 8-passes.

Band contrast (pattern quality) map superimposed on boundary map with high angle boundaries (HABs) of disorientation (θ) greater than 15° as black lines and low angle boundaries (LABs) of $2° < \theta \leq 15°$ as red lines of the 2-pas test is shown in Figure 5(a). It can be seen that the small quasi-polygonal ferrite grains produced by the DT mechanism are separated by HABs and exhibit a low number of LABs in the grain interiors. This observation is well-illustrated by the disorientation line scan from point A to B shown in Figure 5(d). The presence of substructure in these DT ferrite was possibly due to further deformation after the DT ferrite was formed. Conversely, the martensitic areas show a low density of HABs (black) and a high density of LABs (red) on the boundary map due to the shape deformation associated with the displacive transformation that occurred during quenching of the untransformed austenite [41]. Such an example is given by the disorientation profile along the line from C to D shown in Figure 5(d). The corresponding inverse pole figure (IPF) coloured orientation map of the same area is given in Figure 5(b) with the large martensitic area labelled with "M". Furthermore, a "local misorientation map" was produced by using a 5 pixel by 5 pixel filter disregarding disorientations greater than 5° (shown in Figure 5c). The low variations of local orientation (represented by the blue colour) exhibited by the small quasi-polygonal ferrite grains also suggest that they were produced by the DT mechanism and underwent dynamic recovery during further deformation whilst areas with high

local misorientations (green to yellow) are mainly martensite produced from the untransformed austenite.

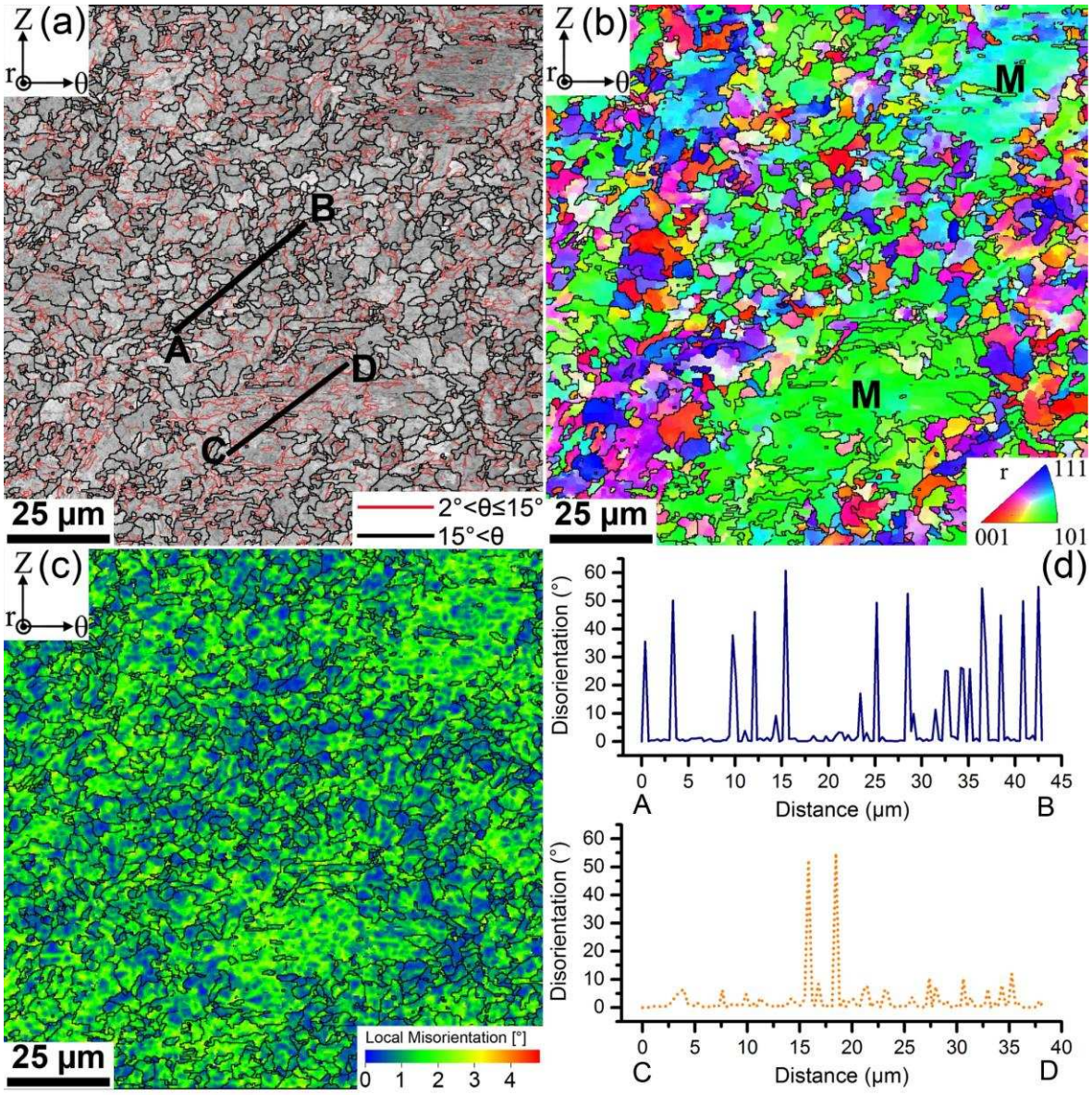

Figure 5: Selected area EBSD maps of the 2-pass deformed specimen at the effective radius: (a) band contrast map superimposed on boundaries map, black line represent high angel boundaries (Θ>15°) and red lines represent low angle boundaries (2°< Θ≤15°); (b) invers pole figure coloured orientation map; (c) local misorientation map produced by a 5-by-5 filter disregarding boundaries with disorientation greater than 5°; (d) disorientation profiles along line A to B and line C to D as shown in (a).

Similarly, the boundary map superimposed with band contrast map, the IPF coloured orientation map and the local misorientation map of the microstructure from the 8-pass test are given in Figure 6(a), (b) and (c), respectively. In this case, the vast majority of the microstructure

consisted of martensite. The disorientation profile of line EF (given in Figure 6d) along the long axis of a martensite lath showed only LABs of disorientation less than 15°. The disorientation line profile of GH across several martensite lathes also revealed similar features, i.e. mainly LABs within the martensite block. These observations are consistent with reported crystallographic features of lath martensite in low-carbon steels [42].

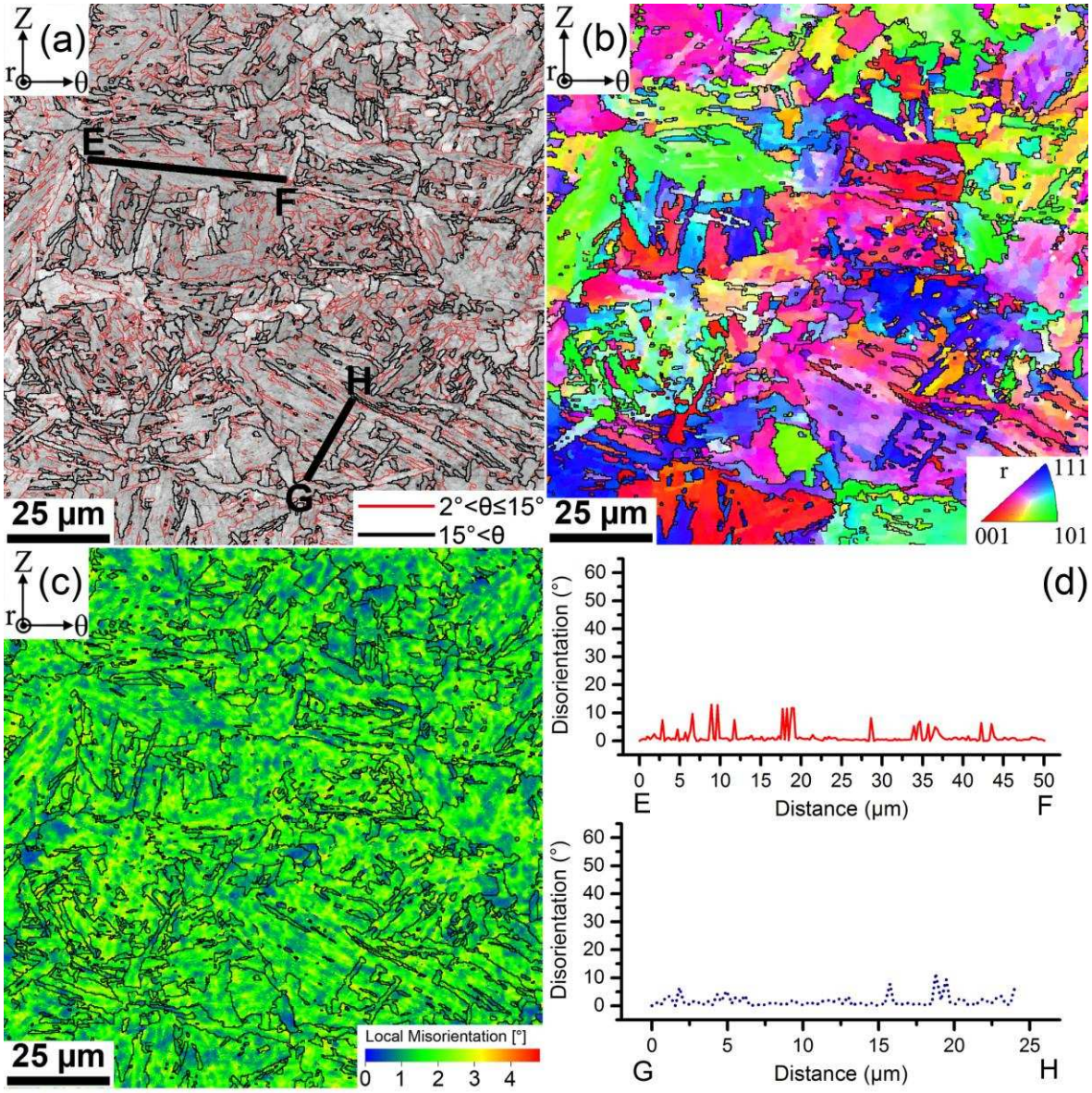

Figure 6: Selected area EBSD maps of the 8-pass deformed specimen at the effective radius: (a) band contrast map superimposed on boundaries map, black line represent high angel boundaries (Θ>15°) and red lines represent low angle boundaries (2°<Θ≤15°); (b) invers pole figure coloured orientation map; (c) local misorientation map produced by a 5-by-5 filter disregarding boundaries with disorientation greater than 5°; (d) disorientation profiles along line E to F and line G to H as shown in (a).

Based on the entire EBSD datasets, the relative frequency of disorientation angles from 4° to 62.8° are plotted as distribution histograms (shown in Figure 7) to reveal the crystallographic boundary characteristics of the microstructures after the 2-pass and the 8-pass tests. The relative frequency of HABs between 15° and 55° are much higher after the 2-pass test than that of the 8-pass test. The substantial amount of DT ferrite formed during the 2-pass test contributed greatly to this high fraction of HABs. For the 8-pass deformed test, the high fraction of LABs is the result of the shape deformation associated with martensitic transformation during quenching. The peaks around 60° of disorientation are believed to due to the specific orientation relationships (OR) required for displacive phase transformations.

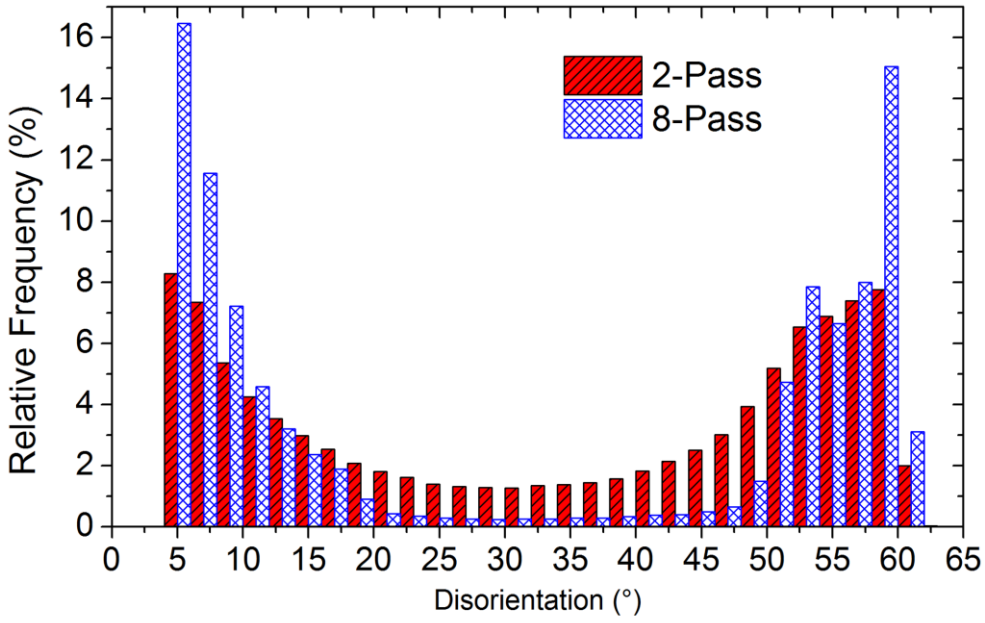

Figure 7: Histograms showing the relative frequency of the magnitude of disorientation angles for the as-quenched microstructures after the 2-pass and 8-pass tests.

All the above microstructural and crystallographic observations indicate an incomplete DT after the 2-pass test and an almost complete suppression of DT after the 8-pass test. Assuming that the critical strains derived by the "double-differentiation" method are reliable, for the 2-pass test, the forward strain to ε_{vm}=1.0 in the first pass was significantly greater than the critical strain $\varepsilon_{C,DT,}$ therefore, allowing DT to be activated. However, for the 8-pass test, the forward strain of ε_{vm}=0.25 was only marginally higher than the $\varepsilon_{C,DT}$ of 0.20, and still below the $\varepsilon_{C,DRX}$ of 0.30. As a result both

DT and DRX were retarded by the subsequent strain reversal. The activation and retardation of DT are believed to be highly dependent on the increment and shape change of the austenite grain boundaries as demonstrated by previous studies. The importance of austenite grain boundaries for DT can be seen more clearly in the following section as the microstructural observations were made near the outer surface the sample gauge at 90% of the gauge radius where the strain experienced by the material was higher than that at the effective radius.

3.3 Microstructure near surface at 90% of the gauge radius (0.9r)

Figure 8(a) and (b) show the micrographs by inverted secondary electron contrast taken at 90% of the gauge radius (0.9r) of the 2-pass test. A majority of the austenite was transformed to very fine DT ferrite, with only a small amount of martensite produced by the displacive decomposition of the remaining austenite (marked by letter M in Figure 8a). The measured volume fraction of DT ferrite at 0.9r is around 90.4%±3.7%, much higher compared to that of 56.5%±7.0% determined at the effect radius (see Table 1). The increased forward strain (ε_{vm}=1.24) and total accumulative strain (ε_{vm}=2.48) at this position are believed to be the main reasons for facilitating further dynamic transformation to produce more DT ferrite.

The microstructures at 0.9r after the 8-pass test are given in Figure 8 (c) and (d). It is clear that there is an increased amount of DT ferrite nucleated primarily at prior-austenite grain boundaries (PAGBs), compared to the microstructure at the effect radius after the same test (Figure 8c and d). The measured volume fraction of DT ferrite is 13.8±1.0%, compared to 2.8±0.9% at the effective radius (see Table 1). Furthermore, the significance of the PAGBs as the nucleation sites for the first generation of DT ferrite grains is nicely demonstrated in Figure 8(d): DT ferrite exhibiting a typical allotriomorphic morphology (labelled as A) populated the PAGBs; the interior of the austenite grains remained untransformed during deformation, and subsequently decomposed to martensite (labelled as M) after quenching. Additionally, certain ferrite grains show a distinctive secondary

Widmanstätten morphology, for example the one labelled as W in Figure 8(d). As the cooling rate is not infinite (~180 °C·s^{-1}) during water quenching which allows the diffusion of carbon, the secondary Widmanstätten ferrite is believed to be developed from existing allotriomorphic DT ferrite that present in the microstructure after deformation. Therefore, these secondary Widmanstätten ferrite were not dynamically but statically transformed by a displacive mechanism after the deformation. The possible transformation mechanism of DT is discussed in Section 4.2.

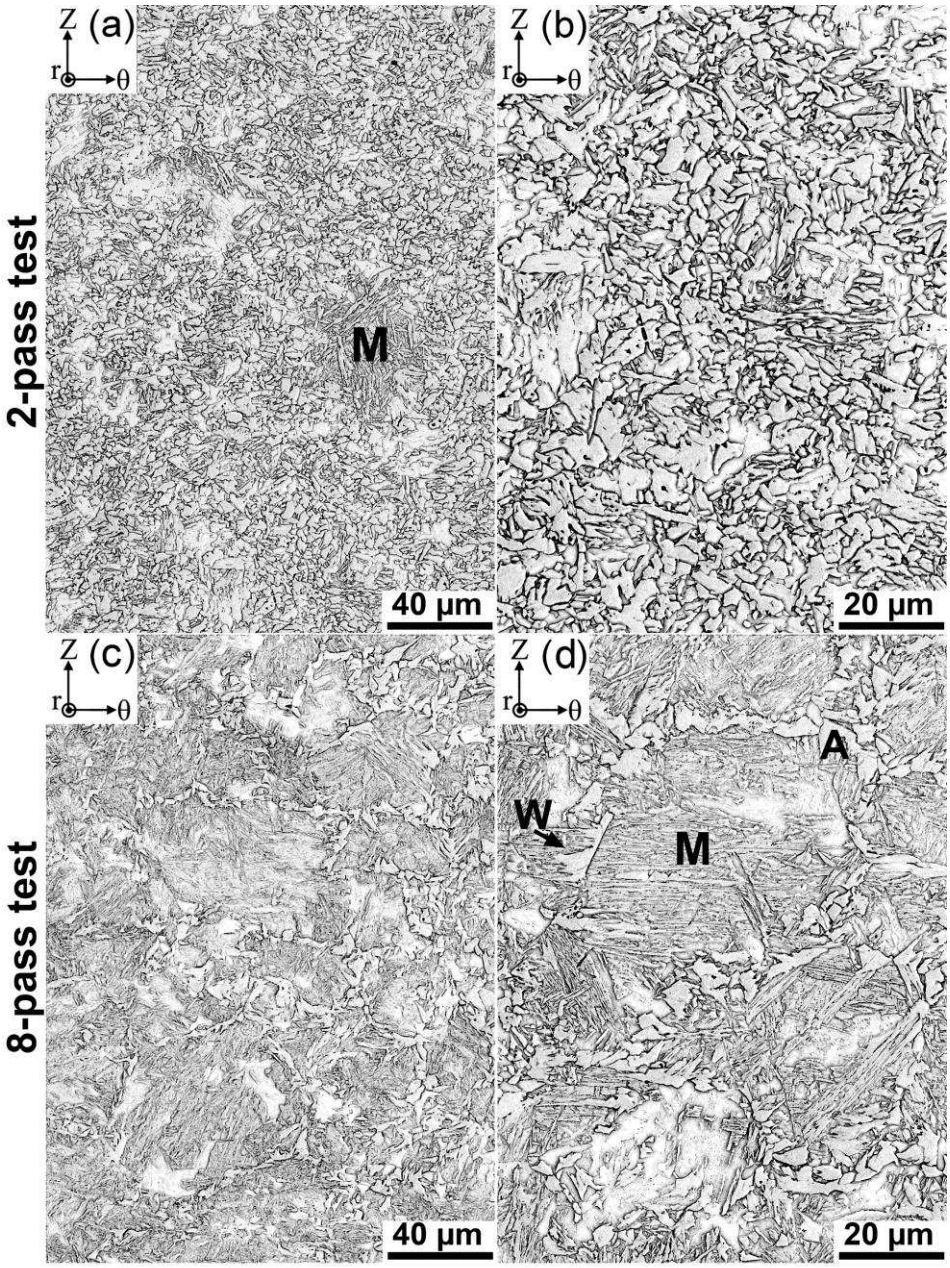

Figure 8: Micrographs showing inverted secondary electron contrast of the microstructure near surface at 90% of the gauge radius in the 2-pass deformed specimen (a and b) and in the 8-pass deformed specimen (c and d).

3.4 The evolution of austenite microstructure revealed by FEM 3D-DMR modelling

Application of a multiscale modelling approach combined together with a 3D digital materials representation provided much more detailed solution regarding strain deformation compared to macroscale simulation as shown in Figure 9. The equivalent plastic strain (PEEQ) distribution at 0.724r and 0.9r after the 7^{th} deformation pass (as indicated by the arrow on the macroscopic flow curve) are given in Figure 9 (c, d) and (e, f), respectively. It can be clearly seen that the solution obtained in the micro-level submodel (Figure 9d and f) provides a much higher resolution of the equivalent plastic strain distribution maps across the deformed microstructures, compared to the results obtained for the strain gauges at the macro-level (Figure 9c and e). It can be seen that the steel deformed at 0.9r undergoes much higher local strains compared to the similar area of the steel deformed at the effective radius of 0.724r.

An implemented modelling approach also allowed for the obtaining of detailed information regarding the deformation gradient at the austenite grain boundaries. Figure 10 presents the strain distribution in selected adjacent austenite grains within unit cells placed at the effective radius (0.724r) and near the torsion specimen's surface (0.9r). It can be clearly observed that not only the strain magnitude but also the strain localisation at the PAGBs is much more significant at 0.9r near the specimen surface (Figure 10h, i) than at the effective radius of 0.724r (Figure 10e, f). These results may explain the reason for the increased amounts of DT ferrite nucleated primarily at the prior-austenite grain boundaries.

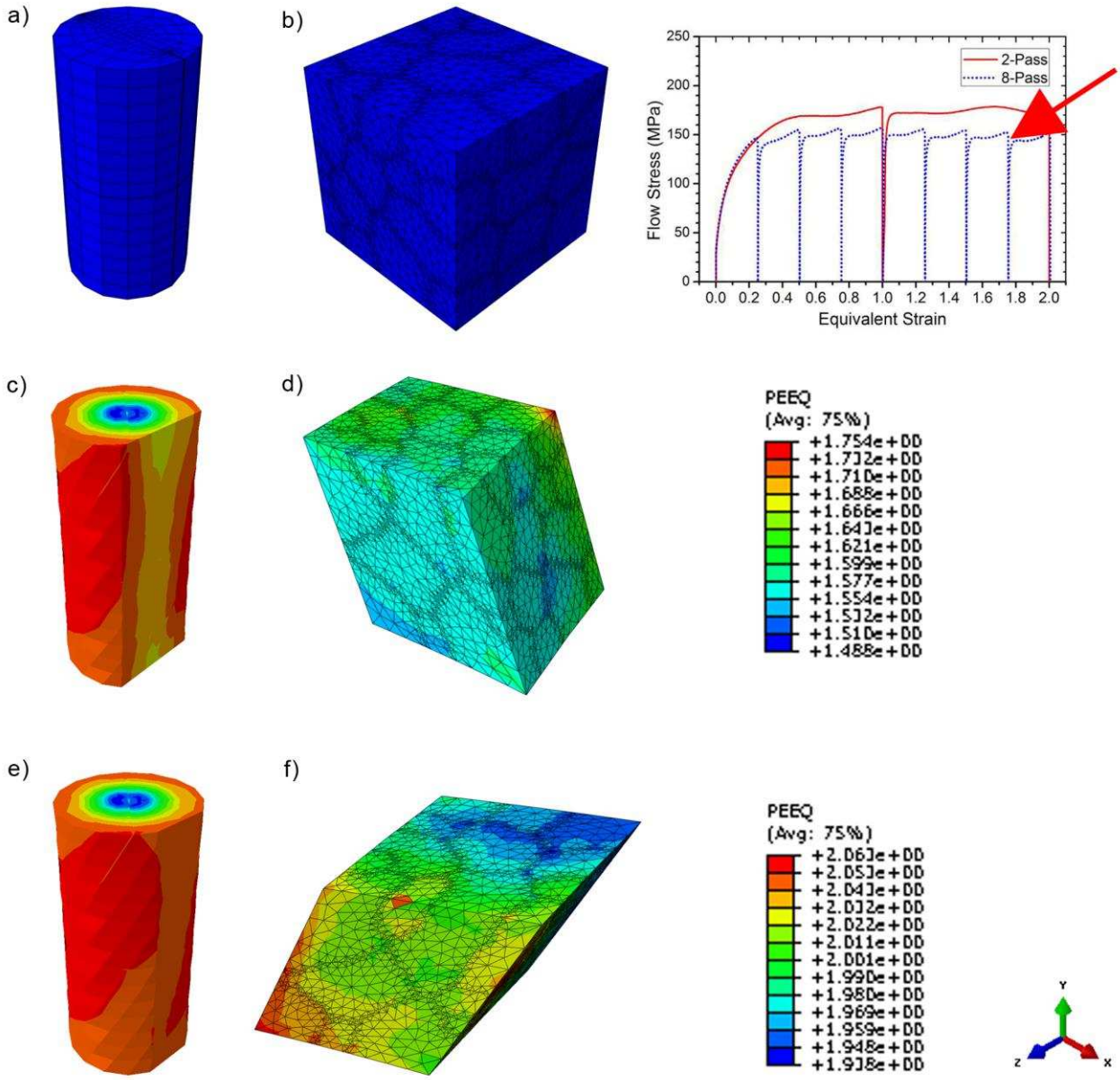

Figure 9: FE mesh in the undeformed strain gauge part of torsion specimen (a) and unit cell (b); Equivalent plastic strain distributions simulated in the 8-pass deformed specimen (after 7 passes) at planes parallel to deformation axis corresponding to 0.724r (c, d) and 0.9r (e, f) in gauge length area(macro level) and unit cells (micro level) respectively.

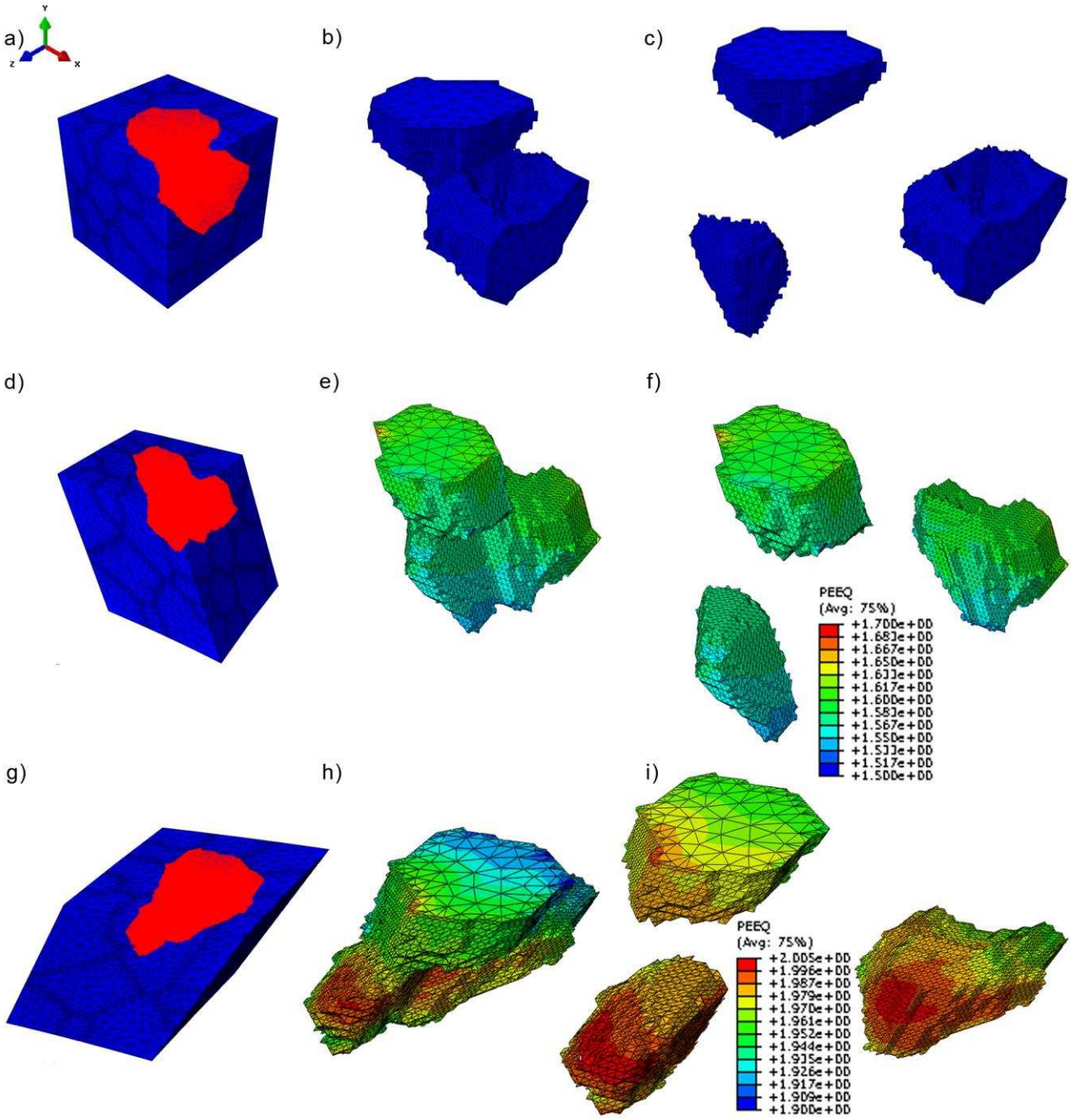

Figure10: Equivalent plastic strain distributions in unit cell and selected prior austenite grains in undeformed specimen (a, b, c) and after 7 passes of deformation at 0.724r (d, e, f) and 0.9r (g, h, i) respectively. Equivalent plastic strain distributions simulated in the 8-pass deformed specimen (after 7 passes) at planes parallel to deformation axis corresponding to 0.724r (c, d) and 0.9r (e, f) in gauge length area (macro level) and unit cells (micro level) respectively.

4 Discussion

4.1 The effect of deformation temperature and the role of PAGBs on DT

Compared to the same material deformed at a lower temperature of 820°C which is about 15°C lower than the measured A_{e3} from a previous study[13], deformation at 920°C (a temperature ~75°C above the measured A_{e3}) in the current study leads to a much smaller amount of DT ferrite, i.e. incomplete transformation (~56% transformed) for the 2-pass deformed steel compared to almost no transformation after the 8-pass deformed steel. Interestingly, the critical strain $\varepsilon_{C,DT}$ at the higher deformation temperature of 920°C is 0.20, smaller than the $\varepsilon_{C,DSIT}$ of 0.50 at 820°C. This observation indicates that the driving force from stored energy of deformation is probably not the key factor to determine the initiation of DT, as the smaller strain ($\varepsilon_{C,DT}$=0.20) at higher temperature (920°C) should result in a lower stored energy, in addition to the already negative chemical driving forcing the γ to α phase transformation (~75°C above the A_{e3}). However, this is based on bulk analysis of the deformation process. On the microstructure level of polycrystalline materials, the deformation is always heterogeneous, especially at the vicinity of the grain boundaries and triple junctions due to compatibility constraints [43]. This type of strain localisation is clearly demonstrated by the FEM 3D-DMR modelling in Section 3.4, which shows higher local accumulated plastic strains near the PAGBs than in the grain interiors (see Figure 10). The high localised strain causes serration and bulging of the PAGBs, which have been shown to be responsible for the initiation of DRX [21, 25, 44] and DSIT [13]. Therefore, at the high deformation temperature of 920°C, the increased tendency for pronounced serration and bulging of the PAGBs, and hence inhomogeneously distributed stored energy, could partly compensate for the low driving force for DT leading to the low critical strain of $\varepsilon_{C,DT}$=0.20 for initiation. A recent review [45] suggests that the transformation mechanism of DT could be a displacive one assisted by mechanical (stress) activation. However, the model was developed assuming homogenous deformation. The results from the current study showed that further consideration and research are

needed to understand the importance of inhomogeneous deformation on DT transformation mechanism.

The observations of incomplete DT after the 2-pass deformation to a total strain of 2.0 together with low critical strain $\varepsilon_{C,DT}$=0.20 for DT initiation suggests that although deforming at a higher temperature above the Ae_3 could reduce the required strains to initiate DT, the total strain (hence rolling reduction) required to complete DT would be much higher. This is probably due partly to other dynamic restoration processes, such as dynamic recovery and DRX of austenite, occurring more rapidly at higher temperatures. For example, from the analysis shown in Figure 3, DRX could be initiated at ~ strain of 0.30 at 920°C. These dynamic restoration processes will compete with the DT process as DRX nucleation also takes place preferentially at serrations and bulgings of the PAGBs. Therefore, the choice of deformation temperature is critical for further industrialisation of DT processing technologies. Suppression of DRX through microalloying could also be beneficial.

4.2 The effect of strain path reversal on DT above Ae_3

Similar to previous work on deformation at temperatures below the Ae_3 [13], the small amplitude of the forward strain at the effective radius (ε_{vm}=0.25) with multiple strain path reversals deformed at temperature above the Ae_3 also leads to the suppression of DT. The mechanism of such suppression is believed to be that the forward strain amplitude of 0.25 is not large enough to cause sufficient serration and bulging of the PAGBs to initiate DT before the reverse straining restoring the grains to their original shape. Therefore, when deformed to the same total accumulated strain of 2.0, the repeated strain path reversals during the 8-pass deformation leads to a very low volume percentage of DT compared to the 2-pass test deformed to the same total accumulative strain.

Near the surface of the gauge radius (0.9r), the strain amplitude of the forward passes are higher than that at the effective radius, generating a ε_{vm} of 0.31 for the 8-pass deformation and a ε_{vm}=1.24 for the 2-pass deformation. As demonstrated by the FEM 3D-DMR modelling results

shown in Figure 10, higher local strains were developed near the PAGBs at 0.9r compared to the effective radius of 0.724r, which in turn caused further serration and bulging of the PAGBs to facilitate the nucleation of DT ferrite. However, it is believed that the amplitude of forward strain in relation to the critical strain of DS initiation ($\varepsilon_{C,DT}$) is the key factor determining the amount of DT ferrite generated after deformation. As shown in Figure 11, there is a good linear correlation between the amplitude of the forward strain and the volume percentage of DT ferrite after the total deformation. More importantly, when extrapolating the linear regression line to 0% DT ferrite, the threshold of ~0.2 for the forward strain amplitude is in good agreement of the $\varepsilon_{C,DT}$ = 0.2 derived from the "double-differentiation" analysis of the flow stress-strain curve (see Figure 3b). The implication is that during multi-pass deformation with full strain path reversals (i.e. the amplitude of forward strain is equal to that of reverse strain whilst the direction is opposite to each other), if the strain amplitude of forward deformation is less than the threshold strain ($\varepsilon_{C,DT}$) of 0.2, no DT could be initiated, even when deformed to very large total accumulated strains. On the other hand, a forward strain amplitude of ε_{vm}=1.44 is required to produce 100% of DT.

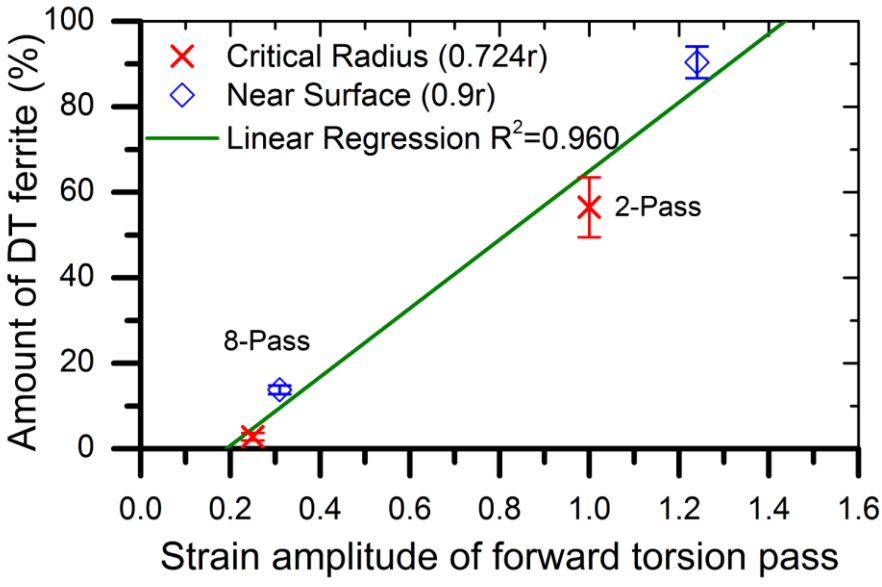

Figure 11: A linear correlation is observed between the strain amplitude of the forward torsion pass during the multipass test and the amount of DT ferrite produced after the whole test.

It is clear that although multiplass deformation at temperatures above the Ae_3 could reduce the demands on the capacity/roll force of the rolling mills to lower the barrier for industrial application of the DT process [3, 4], it also reduces the effectiveness of strain accumulation when strain path changes are involved. Particularly, strain path reversals should be avoided. Furthermore, at higher temperatures, DRX could compete with DT, further reducing the effectiveness of the deformation. Therefore, a careful choice has to be made for the deformation temperature to balance the conflicting demands of reducing roll force for DT and producing a minimal amount of DRX.

5 Conclusions

In the present work, the effect of strain path reversals on DT above the Ae_3 temperature in a microalloyed steel was studied by forward and reverse hot torsion with 2-pass and 8-pass deformations to the same total accumulative strain of 2.0. Flow stress-strain and microstructural analysis, together with FEM modelling by 3D DMR revealed the critical role played by the strain amplitude of the monotonic forward torsion on influencing the evolution of austenite grain boundaries through inhomogeneous deformation, and therefore affecting the DT behaviour of the microalloyed steel. The following conclusions can be made:

1. After both the 8-pass and 2-pass torsional deformation to the total accumulative strain of ε_{vm} =2.0 at 920°C, DT was observed even when the deformation occurred at a temperature ~75°C above the A_{e3}. However, compared to the extensive DT ferrite observed after the 2-pass deformation with a large strain amplitude in each pass (ε_{vm}=1.0) and a single strain path reversal in between, deformation with a small strain amplitude in each pass and multiple strain path reversals, i.e. 8-pass with ε_{vm}=0.25 at each pass, leads to the suppression of DT.
2. Using a modified “double-differentiation” method to analyse the macroscopic flow stress-strain data from the forward torsion of the 2-pass test, critical strains for DT and DRX of

austenite were determined as $\varepsilon_{C,DT}$=0.2 and $\varepsilon_{C,DRX}$=0.3, respectively. The activation of dynamic restoration process such as DRX is believed to compete with the DT process as both DT of ferrite and DRX of austenite take place preferentially at the serrations and bulgings of the PAGBs acting as nucleation sites.

3. During multipass deformation with full strain path reversals, the strain amplitude of the monotonic forward torsion pass was shown to correlate linearly with the amount of DT ferrite produced after the entire deformation process. The small strain amplitudes (0.25 at the effective radius and 0.31 at 0.9r) in each forward pass of the 8-pass test were just above the critical strain of 0.2. Therefore, the forward straining could not cause sufficient serration and bulging of the PAGBs to initiate the DT process leading to a very limited amount of DT ferrite. On the other hand, the large strain amplitude (ε_{vm}=1.0 at effective radius and ε_{vm}=1.24 at 0.9r) during forward torsion of the 2-pass test could cause substantial serration and bulging of PAGBs to facilitate DT, therefore, producing extensive DT.
4. Multipass deformation at temperatures above the A_{e3} could reduce the required roll force, thereby lowering the technological barrier for industrialisation of DT process. However, it also reduces the effectiveness of strain accumulation when strain path changes, in particular full strain path reversals, are involved. Furthermore, at higher deformation temperatures above the A_{e3}, DRX of austenite could be activated to compete with the DT process. This further reduces the effectiveness of straining on DT. Therefore, the choice of an optimal deformation temperature is of critical importance to maximise the benefits from reducing roll force for DT whilst limiting the amount of DRX of austenite that competes with the DT process.

6 Acknowledgements

K Muszka is grateful to National Science Centre, Poland for its financial support through grant No. DEC-2012/05/D/ST8/02367.

7 References

1. Dong, H. and X. Sun, Deformation induced ferrite transformation in low carbon steels. Current Opinion in Solid State and Materials Science, 2005. **9**(6): p. 269-276.
2. Etou, M., et al., Super Short Interval Multi-pass Rolling Process for Ultrafine-grained Hot Strip. ISIJ International, 2008. **48**(8): p. 1142-1147.
3. Kiuchi, M., Integrated production technologies for ultra-fine grained steel sheets. ISIJ International, 2008. **48**(8): p. 1133-1141.
4. Tomida, T., et al., Grain Refinement of C-Mn Steel to 1 μm by Rapid Cooling and Short Interval Multi-pass Hot Rolling in Stable Austenite Region. ISIJ International, 2008. **48**(8): p. 1148-1157.
5. Lee, H.-C. and K.-K. Um, Ferrite Transformation during Deformation of Super-cooled Austenite. ISIJ International, 2008. **48**(8): p. 1050-1055.
6. Li, C.M., H. Yada, and H. Yamagata, In situ observation of $\gamma \rightarrow \alpha$ transformation during hot deformation in an Fe-Ni alloy by an X-ray diffraction method. Scripta Materialia, 1998. **39**(7): p. 963-967.
7. Yada, H., C.M. Li, and H. Yamagata, Dynamic gamma ->alpha transformation during hot deformation in iron-nickel-carbon alloys. ISIJ International, 2000. **40**(2): p. 200-206.
8. Beladi, H., et al., The evolution of ultrafine ferrite formation through dynamic strain-induced transformation. Materials Science and Engineering A, 2004. **371**(1-2): p. 343-352.
9. Beladi, H., et al., Effect of thermomechanical parameters on the critical strain for ultrafine ferrite formation through hot torsion testing. Materials Science and Engineering A, 2004. **367**(1-2): p. 152-161.
10. Beladi, H., G.L. Kelly, and P.D. Hodgson, Ultrafine grained structure formation in steels using dynamic strain induced transformation processing. International Materials Reviews, 2007. **52**(1): p. 14-28.
11. Cai, M.H., H. Ding, and Y.K. Lee, Dynamic Strain-Induced Ferrite Transformation during Hot Compression of Low Carbon Si-Mn Steels. Materials Transactions, 2011. **52**(9): p. 1722-1727.
12. Park, N., et al., Flow stress analysis for determining the critical condition of dynamic ferrite transformation in 6Ni–0.1C steel. Acta Materialia, 2013. **61**(1): p. 163-173.
13. Sun, L., et al., Effect of strain path on dynamic strain-induced transformation in a microalloyed steel. Acta Materialia, 2014. **66**(0): p. 132-149.
14. Poliak, E.I. and J.J. Jonas, A one-parmenter approach to determining the critical conditions for the initiation of dynamic recrystallization. Acta Materialia, 1996. **44**(1): p. 127-136.

15. Basabe, V.V., J.J. Jonas, and H. Mahjoubi, Dynamic Transformation of a Low Carbon Steel at Temperatures above the Ae₃. ISIJ International, 2011. **51**(4): p. 612-618.

16. Basabe, V.V., J.J. Jonas, and C. Ghosh, Formation of Strain-induced Ferrite in Low Carbon Steels at Temperatures Above the Ae₃. ISIJ International, 2013. **53**(12): p. 2233-2241.

17. Ghosh, C., et al., The dynamic transformation of deformed austenite at temperatures above the Ae3. Acta Materialia, 2013. **61**(7): p. 2348-2362.

18. Park, N., et al., Occurrence of dynamic ferrite transformation in low-carbon steel above Ae3. Scripta Materialia, 2013. **68**(7): p. 538-541.

19. Muszka, K., et al., On the effect of strain reversal on static recrystallisation and strain-induced precipitation process kinetics in microalloyed steels. Materials Science Forum, 2012. **715-716**: p. 655-660.

20. Sun, L., et al., The effect of strain path reversal during austenite deformation on phase transformation in a microalloyed steel subjected to accelerated cooling. Materials Science Forum, 2012. **715-716**: p. 667-672.

21. Ponge, D. and G. Gottstein, Necklace formation during dynamic recrystallization: mechanisms and impact on flow behavior. Acta Materialia, 1998. **46**(1): p. 69-80.

22. Fernández, A.I., et al., Dynamic recrystallization behavior covering a wide austenite grain size range in Nb and Nb–Ti microalloyed steels. Materials Science and Engineering A, 2003. **361**(1–2): p. 367-376.

23. Xiao, F.-r., et al., Effect of Nb Solute and NbC Precipitates on Dynamic or Static Recrystallization in Nb Steels. Journal of Iron and Steel Research, International, 2012. **19**(11): p. 52-56.

24. Muszka, K., Modelling of deformation inhomogeneity in the angular accumulative drawing process—multiscale approach. Materials Science and Engineering: A, 2013. **559**(0): p. 635-642.

25. Sun, L., et al., On the interactions between strain path reversal and dynamic recrystallisation in 316L stainless steel studied by hot torsion. Materials Science and Engineering A, 2013. **568**(0): p. 160-170.

26. Barraclough, D.R., et al., Effect of Specimen Geometry on Hot Torsion Test Results for Solid and Tubular Specimens. Journal of Testing and Evaluation, 1973. **1**(3): p. 220-226.

27. Onsoien, M., M. M'hamdi, and A. Mo, A CCT diagram for an offshore pipeline steel of X70 type. AWS Welding Journal, 2009. **88**(1): p. 1s-6s.

28. Cizek, P., et al., Effect of composition and austenite deformation on the transformation characteristics of low-carbon and ultralow-carbon microalloyed steels. Metallurgical and Materials Transactions A, 2002. **33**(5): p. 1331-1349.

29. Sun, L., et al., Mapping microstructure inhomogeneity using electron backscatter diffraction in 316L stainless steel subjected to hot plane strain compression tests. Materials Science and Technology, 2010. **26**(12): p. 1477-1486.

30. Madej, L., et al., Digital Material Representation as an efficient tool for strain inhomogeneities analysis at the micro scale level. Archives of Civil and Mechanical Engineering, 2011. **11**(3): p. 661-679.

31. Muszka, K., L. Madej, and J. Majta, The effects of deformation and microstructure inhomogeneities in the Accumulative Angular Drawing (AAD). Materials Science and Engineering: A, 2013. **574**: p. 68-74.

32. Madej, L., et al., Numerical modeling of dual phase microstructure behavior under deformation conditions on the basis of digital material representation. Computational Materials Science, 2014. **95**: p. 651-662.

33. Szyndler, J. and Ł. Madej, Numerical analysis of the influence of number of grains, FE mesh density and friction coefficient on representativeness aspects of the polycrystalline digital material representation – Plane strain deformation case study. Computational Materials Science, 2015. **96, Part A**: p. 200-213.

34. Lemaitre, J. and J.-L. Chaboche, Mechanics of Solid Materials. 1994, Cambridge, UK: Cambridge University Press.

35. Sun, L., et al., The effect of strain path reversal on high-angle boundary formation by grain subdivision in a model austenitic steel. Scripta Materialia, 2011. **64**(3): p. 280-283.

36. Hasegawa, T., T. Yakou, and S. Karashima, Deformation Behavior and Dislocation-Structures Upon Stress Reversal in Polycrystalline Aluminum. Materials Science and Engineering, 1975. **20**(3): p. 267-276.

37. Cowan, J.R., et al., Recrystallisation following non-proportional straining in aluminium. Materials Science and Technology, 1995. **11**(11): p. 1104-1109.

38. Jonas, J.J., et al., The Avrami kinetics of dynamic recrystallization. Acta Materialia, 2009. **57**(9): p. 2748-2756.

39. Mecking, H. and U.F. Kocks, Kinetics of Flow and Strain-Hardening. Acta Metallurgica, 1981. **29**(11): p. 1865-1875.

40. Jonas, J.J., et al., The Critical Strain for Dynamic Transformation in Hot Deformed Austenite. ISIJ International, 2013. **53**(1): p. 145-151.

41. Bhadeshia, H.K.D.H., Some phase transformations in steels. Materials Science and Technology, 1999. **15**(1): p. 22-29.

42. Kitahara, H., et al., Crystallographic features of lath martensite in low-carbon steel. Acta Materialia, 2006. **54**(5): p. 1279-1288.

43. Raabe, D., et al., Micromechanical and macromechanical effects in grain scale polycrystal plasticity experimentation and simulation. Acta Materialia, 2001. **49**(17): p. 3433-3441.

44. Belyakov, A., H. Miura, and T. Sakai, Dynamic recrystallization under warm deformation of a 304 type austenitic stainless steel. Materials Science and Engineering A, 1998. **255**(1–2): p. 139-147.

45. Ghosh, C., C. Aranas Jr, and J.J. Jonas, Dynamic transformation of deformed austenite at temperatures above the Ae3. Progress in Materials Science, 2016. **82**: p. 151-233.